PHYSICAL REVIEW APPLIED **17,** 034031 (2022)

Planar-Integrated Magneto-Optical Trap

Liang Chen,[1,4] Chang-Jiang Huang,[1,4] Xin-Biao Xu,[1,4] Yi-Chen Zhang,[1,4] Dong-Qi Ma,[1,4]
Zheng-Tian Lu,[2,4] Zhu-Bo Wang,[1,4] Guang-Jie Chen,[1,4] Ji-Zhe Zhang,[1,4] Hong X. Tang,[3]
Chun-Hua Dong,[1,4] Wen Liu,[5] Guo-Yong Xiang,[1,4] Guang-Can Guo,[1,4] and Chang-Ling Zou[1,4,*]

[1] *Key Laboratory of Quantum Information, Chinese Academy of Sciences, University of Science and Technology of China, Hefei, Anhui 230026, People's Republic of China*
[2] *Hefei National Laboratory for Physical Sciences at the Microscale, University of Science and Technology of China, Hefei, Anhui 230026, People's Republic of China*
[3] *Department of Electrical Engineering, Yale University, New Haven, Connecticut 06511, USA*
[4] *CAS Center for Excellence in Quantum Information and Quantum Physics, University of Science and Technology of China, Hefei, Anhui 230026, People's Republic of China*
[5] *USTC Center for Micro- and Nanoscale Research and Fabrication, University of Science and Technology of China, Hefei, Anhui 230026, People's Republic of China*

(Received 25 July 2021; revised 19 January 2022; accepted 28 February 2022; published 10 March 2022)

The magneto-optical trap (MOT) is an essential tool for collecting and preparing cold atoms with a wide range of applications. We demonstrate a planar-integrated MOT by combining an optical grating chip with a magnetic coil chip. The flat grating chip simplifies the conventional six-beam configuration down to a single laser beam, and the flat coil chip replaces the conventional anti-Helmholtz coils of cylindrical geometry. Up to 10^6 cold ^{87}Rb atoms are trapped by the planar-integrated MOT, with the atom cloud being approximately 6 mm above the chip surface. This configuration effectively reduces the volume, weight, and complexity of the MOT, bringing benefits to applications including gravimeter, clock, and quantum memory devices.

DOI: 10.1103/PhysRevApplied.17.034031

I. INTRODUCTION

The magneto-optical trap (MOT) is one of the most important experimental platforms in atomic physics [1–4]. Cold atoms prepared by an MOT are widely used in quantum measurement and metrology applications [5–7]. For example, atomic gravimetry with precision achieving $\mu\mathrm{Gal}/\sqrt{\mathrm{Hz}}$ has been demonstrated [8]. The conventional MOT apparatus consists of three orthogonal pairs of retroreflected laser beams and a pair of anti-Helmholtz coils in cylindrical geometry [9].

Over the past decade, great efforts have been devoted to minimizing the MOT system. For example, by using a pyramidal retroreflector, only one incident laser beam is needed [10–13]. More recently, this idea was further developed by replacing the pyramidal retroreflector with a completely flat chip consisting of three gratings [14–21]. At the same time, the cumbersome vacuum system has been successfully miniaturized to cubic centimeter scale, retaining compatibility with the grating MOT configuration [22,23]. In contrast, the original bulky anti-Helmholtz coils still remain. Although U- or Z-shaped wires are employed in an atom chip to assist the MOT, external Helmholtz coils are still required to provide a bias field [12,13,24–27].

In this work, we develop a planar-integrated MOT (piMOT) configuration based on both a grating chip and a planar 3 cm × 3 cm coil chip. The coil chip generates a quadrupole magnetic field several millimeters above the chip surface, matching the working point of the optical grating chip. While carrying a current of 2.0 A, the coil chip generates a magnetic field with gradient reaching 13.9 G/cm, with a low working voltage of 3.2 V and a low power of 6.4 W. With both chips stacked outside a glass vacuum cell, we trap 10^6 ^{87}Rb atoms. The piMOT is simple, portable, and low-cost. It opens the possibility for further monolithic integration of the cold-atom system with photonic chips [28–31], with future applications including portable gravimeter [32–35], clock [36–40], and quantum memory devices [41–44].

II. THE COIL CHIP

In the MOT configuration, the atoms are trapped at the working point where the magnetic field equals zero and strong magnetic field gradients are present in all directions [45]. A conventional MOT generates this magnetic field

---

[*] clzou321@ustc.edu.cn

using a pair of anti-Helmholtz coils [9], which is composed of a pair of identical coils (same radius R, current I, and number of turns N) with opposite current directions, as shown in Fig. 1(a). The working point of this coil configuration is exactly its geometrical center. This cylindrical geometry imposes limitations on a compact cold-atom system. For example, the vacuum cell needs to be inserted in between the pair of coils, thus limiting the minimum size of the coils. In order to achieve the required field gradient of approximately 10 G/cm, the required currents in the coils grow with the cube of the coil size, which then leads to heat dissipation problems. These limitations can be overcome with a planar coil design to achieve a more compact system.

We propose the coplanar annular coil chip [Fig. 1(b)], consisting of two coaxial coils with different radii R_1 and R_2 ($R_1 < R_2$), different numbers of turns N_1 and N_2, and opposite currents I and $-I$. Here, we define the center of the coils as the origin of the circular coordinate system and the z axis perpendicular to the coil plane. At a point ($\rho = 0$, φ, $z = z_0$) on the z axis, the coils produce a magnetic field intensity $\mathbf{B} = \left(B_\rho,\ B_\varphi = 0,\ B_z\right)$ as [45]

$$B_z\left(0,\varphi,z_0\right) = \frac{\mu_0 I}{2}\left(\frac{N_1R_1^2}{\left(R_1^2+z_0^2\right)^{\frac{3}{2}}} - \frac{N_2R_2^2}{\left(R_2^2+z_0^2\right)^{\frac{3}{2}}}\right), \tag{1}$$

$$B_\rho\left(0,\varphi,z_0\right) = 0, \tag{2}$$

and the corresponding magnetic field gradients are

$$\frac{\partial B_z}{\partial z}\left(0,\varphi,z_0\right) = -\frac{3\mu_0 z_0 I}{2}\left(\frac{N_1R_1^2}{\left(R_1^2+z_0^2\right)^{\frac{5}{2}}} - \frac{N_2R_2^2}{\left(R_2^2+z_0^2\right)^{\frac{5}{2}}}\right), \tag{3}$$

$$\frac{\partial B_\rho}{\partial \rho}\left(0,\varphi,z_0\right) = \frac{3\mu_0 z_0 I}{4}\left(\frac{N_1R_1^2}{\left(R_1^2+z_0^2\right)^{\frac{5}{2}}} - \frac{N_2R_2^2}{\left(R_2^2+z_0^2\right)^{\frac{5}{2}}}\right). \tag{4}$$

Due to the cylindrical symmetry, $\partial B_\rho/\partial\rho = -\frac{1}{2}\partial B_z/\partial z$ on the z axis. For appropriate R_1 and R_2, we can adjust N_1 and N_2 to make the field intensities zero at a desired height h, namely, at the target MOT working point $(0, 0, h)$. As a result, this coplanar coil configuration is able to provide the quadrupole magnetic field for realizing an MOT, with the working point above the surface of the coil plane.

A practical coil chip is constructed based on printed-circuit-board technology, with a chip thickness of 700 μm and an edge length of 3 cm [Fig. 1(c)]. The chip consists of three layers of identical copper circuits connected in parallel. The thickness, width, and spacing of the printed copper wire are 70 μm, 200 μm, and 200 μm, respectively. The inner coil on each layer has $N_1 = 17$ turns, with a radius ranging from 2.0 mm to 8.8 mm, and the outer coil has $N_2 = 13$ turns, with a radius ranging from 9.6 mm to 14.8 mm. Circuit ends are connected to printed pads on the bottom side of the chip through metallized holes. This configuration allows the current supply wires to be welded to the bottom side of the chip, thus preventing them from influencing the magnetic field above

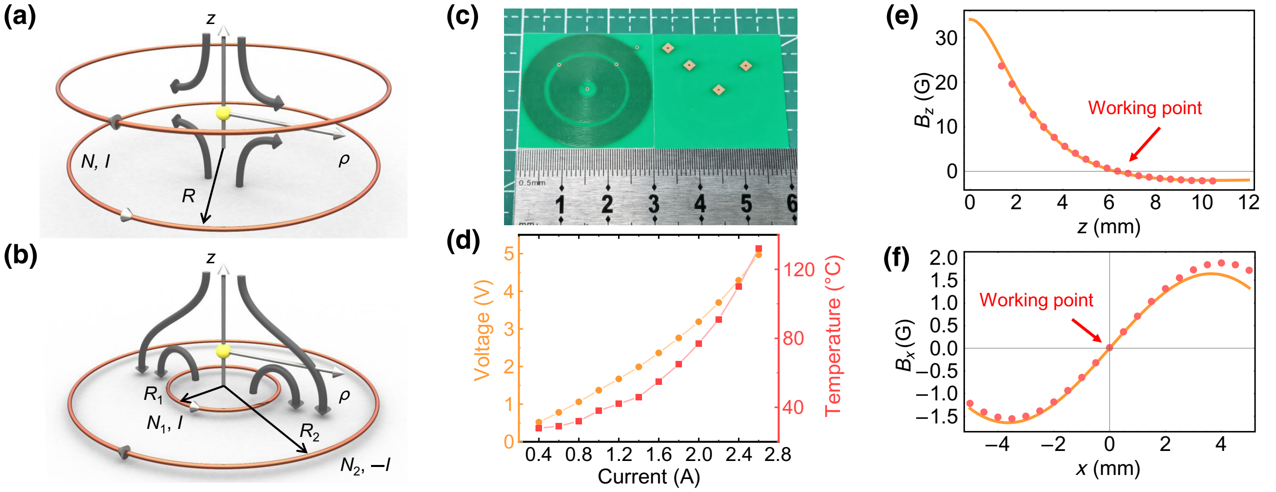

FIG. 1. The planar quadrupole-field coil chip. (a) Conventional anti-Helmholtz coils in three-dimensional cylindrical geometry. (b) Planar coils. Parameters R, N, I are the radii, numbers of turns, and current of each annular coil, respectively. The magnetic field lines are indicated by the gray curves. (c) Top and bottom view of a practical coil chip. (d) Steady-state voltage and temperature of the coil chip versus the applied currents. (e),(f) Calculated (orange line) and measured (red points) results of the magnetic field components along z and x axes.

the chip. According to Eqs. (1)–(4), this coil chip has a working point at a height of $h = 6.3$ mm, an axial field gradient of $\partial B_z/\partial z = 13.9$ G/cm, and a radial gradient of $\partial B_\rho/\partial \rho = -7.0$ G/cm when these three layers carry a total current of $I = 2.0$ A. We choose a ρz plane with an arbitrary ϕ, and investigate the magnetic field distribution by theoretically calculation and experimental measurement. For the convenience of description and measurement, we redefine a xz rectangular coordinate system on this plane, setting the center of the coils as the origin, and the z axis perpendicular to the coil plane. The dependence of B_x on x could equivalently replace the dependence of B_ρ on ρ by the relation $\rho = |x|$. Figures 1(e) and 1(f) show the well-matched calculated (orange line) and measured (red points) results of the axial and radial magnetic fields (B_z and B_x). From the measured field distribution, within a range of about 2 mm in both the $\pm\, x$ and $+z$ directions around the working point, the coil chip can provide the desired magnetic field gradients for the MOT.

Besides the magnetic fields, we evaluate the performance of the coil chip for practical applications by measuring the steady-state voltage and temperature of the chip versus the current I [Fig. 1(d)]. At the working current $I = 2.0$ A, the voltage is measured as 3.2 V. Under a low heating power of 6.4 W, the chip temperature could remain at around 77°C. Therefore, the coil chip can provide a stable magnetic field for MOT at a low power setting, which is made possible by the small size and consequently the small resistance in the planar-integrated design.

III. EXPERIMENTAL PERFORMANCE OF THE PLANAR-INTEGRATED MOT

Figure 2(a) shows a conceptual sketch of the piMOT based on the combination of a grating chip [Fig. 2(b)] and a coil chip [Fig. 1(c)]. The grating chip consists of three etched gratings on a silicon substrate. Following pioneering work on the grating MOT [15,19], the angle between grating periodic directions is 120°, and the grating period and duty cycle are 1.10 μm and 0.454, respectively [Figs. 2(c) and 2(d)]. The top side of the grating chip is gold-coated to increase diffraction efficiency. The measured diffraction angle is 45° with respect to z axis and the diffraction efficiency is 40%.

In our experiment, the grating chip is mounted underneath and outside the vacuum cell. The coil chip is mounted below the grating chip and aligned so that the two working points of the chips coincide. Two external-cavity diode lasers are tuned to the 780 nm ^{87}Rb D2 lines. The cooling laser frequency is tuned to the $^5\mathrm{S}_{1/2}(F = 2)$ to $^5\mathrm{P}_{3/2}(F' = 3)$ cycling transition with a red detuning of about -9 MHz, and the repump laser is tuned to the $^5\mathrm{S}_{1/2}(F = 1)$ to $^5\mathrm{P}_{3/2}(F' = 2)$ transition. The beams of the two lasers are combined and coupled into a polarization-maintaining fiber and delivered to the MOT setup. The incident beam is circularly polarized, with a diameter of 3.0 cm, and an optical intensity of 20 mW/cm^2 for the cooling laser and 2 mW/cm^2 for the repump. Three first-order diffraction beams from the gratings along with the incident beam form an MOT in the presence of a quadrupole magnetic field [see Fig. 2(a)].

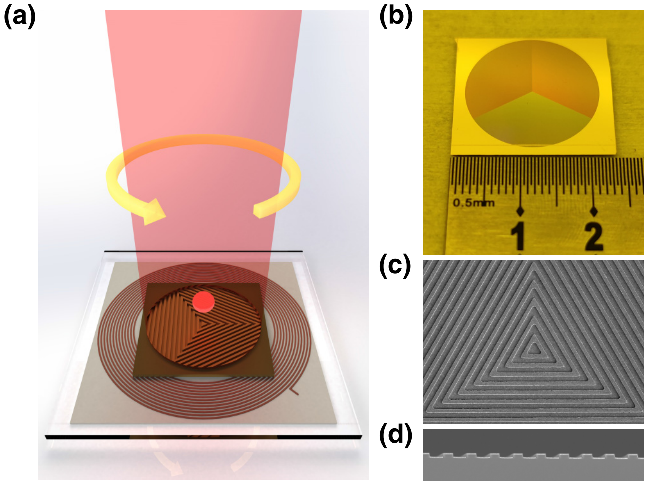

FIG. 2. Experimental apparatus of the planar-integrated MOT. (a) Conceptual sketch of the planar-integrated MOT. The left-handed incident laser beam propagates perpendicular to the grating chip and traps a cold-atom cloud in the presence of the coil chip. (b) The grating chip. (c),(d) Scanning electron microscope (SEM) pictures of the grating chip in a top/side view.

By absorption imaging and time-of-flight method, the temperature of the trapped atom cloud is evaluated. Figure 3(a) shows the absorption images of cold atoms following free expansion over a duration t. Figure 3(b) shows the experimental and fitting results of the atom cloud sizes against t. The extracted temperature is 382 μK for the axial direction and 1.37 mK for the radial direction. Moreover, we adjust the cooling laser intensity and the magnetic field gradient to examine the system performance, and the results are summarized in Fig. 3(c). At a trapping laser intensity of 20 mW/cm^2, the piMOT achieves an atom number of 2.3×10^6 and a number density around 7×10^9 cm^{-3}.

IV. DEPENDENCE OF THE MOT PERFORMANCE ON COOLING LASER DETUNING AND COIL CHIP CURRENT

The dependence of MOT performance on cooling laser detuning and coil chip current is investigated. As shown in Fig. 4, the total atom number (red points) and atom cloud radius (purple points) at different coil chip currents I are measured by scanning the cooling laser detuning (Δ) with respect to the $^5\mathrm{S}_{1/2}(F = 2)$ to $^5\mathrm{P}_{3/2}(F' = 3)$ transition. For a given I, there exists an optimal detuning $\Delta_{\mathrm{opt},N}$ for achieving largest atom number N, and an optimal detuning $\Delta_{\mathrm{opt},\sigma}$ when observing largest atom cloud radius σ. Both

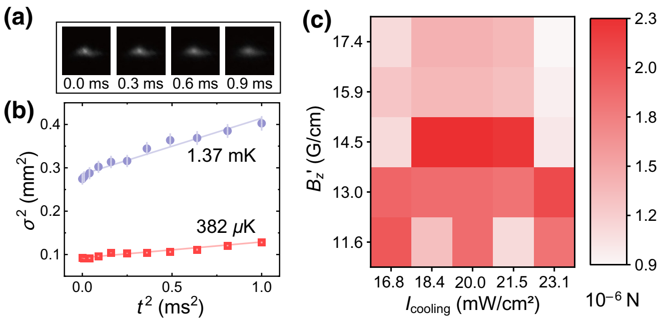

FIG. 3. Experimental performance of the planar-integrated MOT. (a) Several absorption images of MOT atoms after free expansion over different times t. (b) The fitted squared 1/e radii of the ^{87}Rb cloud in the axial (red points) and radial (purple points) directions versus the squared time t^2. Two lines are the fits of $\sigma^2 = \sigma_0^2 + k_B T t^2/m$ to the data, where σ is the 1/e radii of the ^{87}Rb cloud in the axial (red line) and radial (purple line) directions, k_B is the Boltzmann constant, T is the temperature, and m is the mass of an ^{87}Rb atom. (c) Atom number N versus input cooling laser intensity I_{cooling} and axial magnetic field gradient B_z'.

$\Delta_{\text{opt},N}$ and $\Delta_{\text{opt},\sigma}$ decrease monotonously with I, and the relationship between $\Delta_{\text{opt},N}$ (red points), $\Delta_{\text{opt},\sigma}$ (purple points), and I is plotted in Fig. 5(a).

We attribute such a relation between optimal cooling laser detuning and coil chip current to the irregular magnetic field distribution generated by our coil chip [Figs. 1(e) and 1(f)]. To illustrate the principle, Fig. 5(b) shows the simplified model of energy levels in our MOT [9] in the x-direction [Fig. 1(f)]. The bottom black solid line represents a spin $S = 0$ ($m_S = 0$) ground state, and the top three black solid lines represent a spin $S = 1$ ($m_S = -1, 0, +1$) excited state, which shows spatially dependent Zeeman energy shifts proportional to the magnetic field. The red dashed line indicates the cooling laser frequency, which is red-detuned from the $S = 0$, $m_S = 0$ state to induce restoring force in the presence of quadrupole magnetic field [9]. At the cross points between the black lines and the red line, the atoms are on-resonance with the laser and thus the restoring force reaches its maximum. Therefore, atoms could be bounced back at the cross points, and the cross point could be treated as a "barrier," as depicted by the yellow arrows in Fig. 5(b). If the detuning is too large so that the red line has no cross points over black lines, the "barriers" would locate where detuning is most compensated, and be weaker because the exceeding part of detuning beyond the Zeeman shift leads to a reduction in restoring force [see Fig. 5(c)]. We conjecture that the near-optimal total atom number would be achieved when the volume between two "barriers" is maximized while keeping the maximum restoring force on two "barriers" simultaneously. Therefore, it would be preferable to set the detuning coincident with the lower bound of Zeeman shift, as shown by Fig. 5(d).

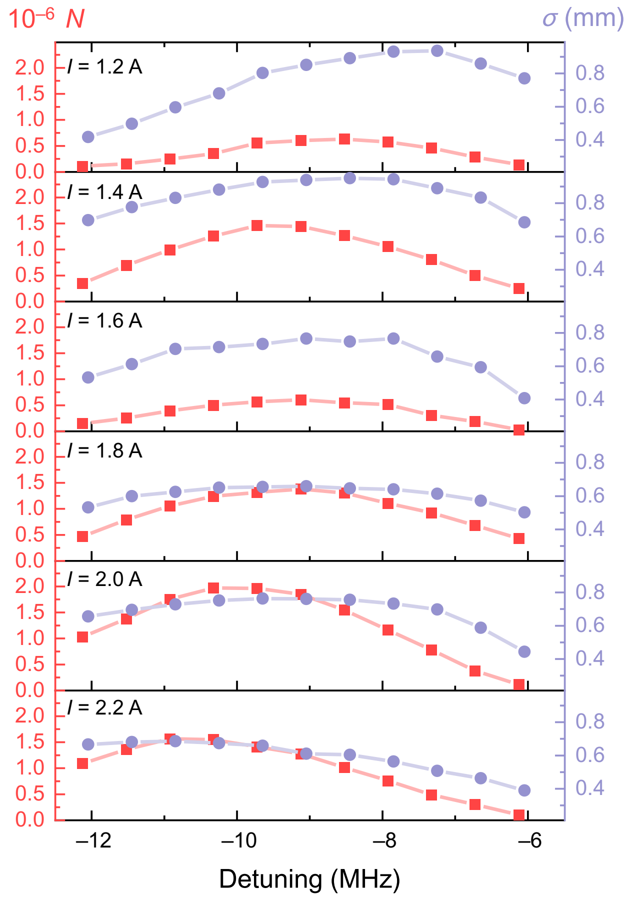

FIG. 4. The total number N and radius σ of the atom cloud against the cooling laser detuning for various coil chip currents I.

According to this conjecture, we could theoretically predict an optimal detuning $\Delta_{\text{opt},p}$. With the magnetic field distribution of our chip [Figs. 1(e) and 1(f)], the tuning points of the magnetic fields (corresponding to the "barrier") have an approximate amplitude $B \sim (0.9 \pm 0.1)$ G/A $\times I$ when considering the distributions in the $\pm x$- and $+z$-directions. For the dominant transitions in our MOT ($F = 2$, $m_F = \pm 2$ to $F = 3$, $m_F = \pm 3$), the transition frequency varies with magnetic field as $\partial f/\partial B \approx (3 \times 0.93 - 2 \times 0.7) = 1.39$ MHz/G, due to the difference between the Zeeman coefficients of the upper and lower levels [46]. Hence, the optimal detuning could be derived as $\Delta_{\text{opt},p} \approx B\partial f/\partial B = (1.25 \pm 0.14)$ MHz/A $\times$ I, showing a linear dependence on I. As shown in Fig. 5(a), our predicted $\Delta_{\text{opt},p}$ agrees with the experimental results without any fitting parameter.

V. DISCUSSION

By replacing the bulky anti-Helmholtz coils in a conventional MOT setup with our planar-designed coil chip, the cold-atom setup could be greatly simplified. The

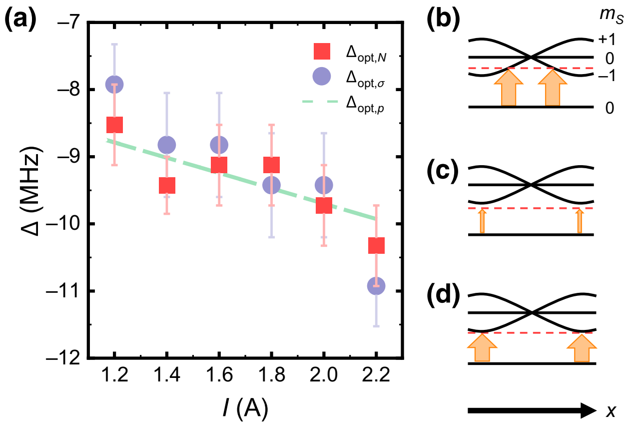

FIG. 5. Dependence of the detuning on coil chip current. (a) Optimal detuning $\Delta_{\mathrm{opt},N}$ for achieving the largest atom number N, optimal detuning $\Delta_{\mathrm{opt},\sigma}$ when observing the largest atom cloud radius σ, and predicted optimal detuning $\Delta_{\mathrm{opt},p}$ versus coil chip current I. (b),(c),(d) Simplified conceptual sketches of the MOT when cooling laser detuning is within, beyond, and coincident with the lower bound of the Zeeman shift. The bottom black solid line represents a spin $S = 0$ ($m_S = 0$) ground state, and the top three black solid lines represent a spin $S = 1$ ($m_S = -1, 0, +1$) excited state. The red dashed line indicates the cooling laser frequency, which is red-detuned from the $S = 0$, $m_S = 0$ state. The yellow arrows indicate "barriers" where detuning is most compensated.

compact piMOT system would benefit a wide range of related applications of cold atoms, including portable precision measurement systems and miniaturized quantum computing systems. Our preliminary results encourage further exploration of the coil chip, and many questions need to be considered.

First, the coil chip is specially designed for a miniaturized cold-atom system, resulting in some fundamental limitations. The working range of the magnetic field is approximately 2 mm in the ± x and $+z$ directions from the center, which would eventually limit the atom cloud radius and total atom number. Meanwhile, the height of the working point is less than 10 mm, and might be troublesome when considering the potential influence of the cell wall.

Second, the performance of the piMOT could be further optimized. Although the microkelvin-level temperature of the trapped atoms is common for the grating-based MOT [15], 10-μK-level or even lower temperatures are highly desired for practical applications. This problem could be improved by adding an extra sub-Doppler cooling stage after the MOT loading [14–17]. Moreover, the phase-space density could be improved by choosing an appropriate cooling laser intensity and designing grating chips with a proper diffraction angle [17].

Finally, the design of piMOT is flexible and could be extended to other coil configurations. In this work, the two chips are nontransparent and thus prevent laser beams from transmitting through chips from the vertical direction. For potential applications of cold-atom interferometers [8], apertures could be introduced to the center of the chips to allow the counterpropagating Raman beams. As demonstrated in previous work [21,31,47], the grating chip is compatible with a hole. In addition, the configuration of the coil circuit is very flexible and could be designed to construct more complex magnetic-field distributions. For example, the coil circuits could be printed in ellipses to capture a cigar-shaped cold-atom cloud, which could enhance the optical depth for quantum memory devices [41–44]. Besides, the coil chip can be designed with several inner coils arranged inside a single outer coil to create an atom cloud array [12,13,20], which might attract research interest in the gradiometry, quantum computing, and simulation communities [48–50].

VI. CONCLUSION

We have demonstrated a planar coil configuration to provide a quadrupole magnetic field for realizing a chip-based MOT. Combining two chips, for magnetic coil and optical grating, the planar-integrated MOT is realized, with significantly reduced volume and weight. This configuration allows more optical access and reduces the power requirements on the current supply and heat dissipation. Therefore, the piMOT holds great potential for applications with portable cold-atom systems. Our system also shows excellent compatibility with photonic chips and convenience in alignment, providing an important solution toward a fully integrated cold-atom system for sensors and quantum devices.

ACKNOWLEDGMENTS

We would like to thank Tianchu Li, Yang Yang, and Xiaochi Liu for helpful discussions, and Yuanhao Yang for helping take SEM pictures of the grating chip. The work was supported by the National Key Research and Development Program of China (Grants No. 2016YFA0302200 and No. 2016YFA0301303), the National Natural Science Foundation of China (Grants No. 11922411, No. 11874342, No. 41727901, No. U21A20433, and No. U21A6006), the Fundamental Research Funds for the Central Universities, and Open Research Funding from Division of Time and Frequency in the National Institute of Metrology (Grant No. AKYKF2107). This work was partially carried out at the USTC Center for Micro and Nanoscale Research and Fabrication.

---

[1] H. Zhai, Degenerate quantum gases with spin-orbit coupling: A review, Rep. Prog. Phys. **78**, 026001 (2015).

[2] O. Firstenberg, C. S. Adams, and S. Hofferberth, Nonlinear quantum optics mediated by Rydberg interactions, J. Phys. B **49**, 152003 (2016).

[3] N. R. Cooper, J. Dalibard, and I. B. Spielman, Topological bands for ultracold atoms, Rev. Mod. Phys. **91**, 015005 (2019).

[4] M. Tomza, K. Jachymski, R. Gerritsma, A. Negretti, T. Calarco, Z. Idziaszek, and P. S. Julienne, Cold hybrid ion-atom systems, Rev. Mod. Phys. **91**, 035001 (2019).

[5] L. Liu *et al.*, In-orbit operation of an atomic clock based on laser-cooled 87Rb atoms, Nat. Commun. **9**, 2760 (2018).

[6] J. Grotti *et al.*, Geodesy and metrology with a transportable optical clock, Nat. Phys. **14**, 437 (2018).

[7] T. Udem, R. Holzwarth, and T. W. Hänsch, Optical frequency metrology, Nature **416**, 233 (2002).

[8] Z.-K. Hu, B.-L. Sun, X.-C. Duan, M.-K. Zhou, L.-L. Chen, S. Zhan, Q.-Z. Zhang, and J. Luo, Demonstration of an ultrahigh-sensitivity atom-interferometry absolute gravimeter, Phys. Rev. A **88**, 043610 (2013).

[9] E. L. Raab, M. Prentiss, A. Cable, S. Chu, and D. E. Pritchard, Trapping of Neutral Sodium Atoms with Radiation Pressure, Phys. Rev. Lett. **59**, 2631 (1987).

[10] K. I. Lee, J. A. Kim, H. R. Noh, and W. Jhe, Single-beam atom trap in a pyramidal and conical hollow mirror, Opt. Lett. **21**, 1177 (1996).

[11] M. Vangeleyn, P. F. Griffin, E. Riis, and A. S. Arnold, Single-laser, one beam, tetrahedral magneto-optical trap, Opt. Express **17**, 13601 (2009).

[12] S. Pollock, J. P. Cotter, A. Laliotis, and E. A. Hinds, Integrated magneto-optical traps on a chip using silicon pyramid structures, Opt. Express **17**, 14109 (2009).

[13] S. Pollock, J. P. Cotter, A. Laliotis, F. Ramirez-Martinez, and E. A. Hinds, Characteristics of integrated magneto-optical traps for atom chips, New J. Phys. **13**, 043029 (2011).

[14] M. Vangeleyn, P. F. Griffin, E. Riis, and A. S. Arnold, Laser cooling with a single laser beam and a planar diffractor, Opt. Lett. **35**, 3453 (2010).

[15] C. C. Nshii, M. Vangeleyn, J. P. Cotter, P. F. Griffin, E. A. Hinds, C. N. Ironside, P. See, A. G. Sinclair, E. Riis, and A. S. Arnold, A surface-patterned chip as a strong source of ultracold atoms for quantum technologies, Nat. Nanotechnol. **8**, 321 (2013).

[16] J. Lee, J. A. Grover, L. A. Orozco, and S. L. Rolston, Sub-doppler cooling of neutral atoms in a grating magneto-optical trap, J. Opt. Soc. Am. B **30**, 2869 (2013).

[17] J. P. McGilligan, P. F. Griffin, E. Riis, and A. S. Arnold, Phase-space properties of magneto-optical traps utilising micro-fabricated gratings, Opt. Express **23**, 8948 (2015).

[18] J. P. McGilligan, P. F. Griffin, E. Riis, and A. S. Arnold, Diffraction-grating characterization for cold-atom experiments, J. Opt. Soc. Am. B **33**, 1271 (2016).

[19] J. P. Cotter, J. P. McGilligan, P. F. Griffin, I. M. Rabey, K. Docherty, E. Riis, A. S. Arnold, and E. A. Hinds, Design and fabrication of diffractive atom chips for laser cooling and trapping, Appl. Phys. B **122**, 172 (2016).

[20] J. P. McGilligan, P. F. Griffin, R. Elvin, S. J. Ingleby, E. Riis, and A. S. Arnold, Grating chips for quantum technologies, Sci. Rep. **7**, 384 (2017).

[21] D. S. Barker, E. B. Norrgard, N. N. Klimov, J. A. Fedchak, J. Scherschligt, and S. Eckel, Single-Beam Zeeman Slower and Magneto-Optical Trap Using a Nanofabricated Grating, Phys. Rev. Appl. **11**, 064023 (2019).

[22] J. P. McGilligan, K. R. Moore, A. Dellis, G. D. Martinez, E. de Clercq, P. F. Griffin, A. S. Arnold, E. Riis, R. Boudot, and J. Kitching, Laser cooling in a chip-scale platform, Appl. Phys. Lett. **117**, 054001 (2020).

[23] O. S. Burrow, P. F. Osborn, E. Boughton, F. Mirando, D. P. Burt, P. F. Griffin, A. S. Arnold, and E. Riis, Stand-alone vacuum cell for compact ultracold quantum technologies, Appl. Phys. Lett. **119**, 124002 (2021).

[24] J. Reichel, W. Hänsel, and T. W. Hänsch, Atomic Micromanipulation with Magnetic Surface Traps, Phys. Rev. Lett. **83**, 3398 (1999).

[25] J. Denschlag, D. Cassettari, and J. Schmiedmayer, Guiding Neutral Atoms with a Wire, Phys. Rev. Lett. **82**, 2014 (1999).

[26] R. Folman, P. Krüger, D. Cassettari, B. Hessmo, T. Maier, and J. Schmiedmayer, Controlling Cold Atoms Using Nanofabricated Surfaces: Atom Chips, Phys. Rev. Lett. **84**, 4749 (2000).

[27] J. Rushton, R. Roy, J. Bateman, and M. Himsworth, A dynamic magneto-optical trap for atom chips, New J. Phys. **18**, 113020 (2016).

[28] J. Xie, J.-Q. Wang, Z.-B. Wang, X.-X. Hu, X. Guo, R. Niu, J. B. Surya, J.-Z. Zhang, C.-H. Dong, G.-C. Guo, H. X. Tang, and C.-L. Zou, Infrared laser locking to a rubidium saturated absorption spectrum via a photonic chip frequency doubler, Opt. Lett. **44**, 1150 (2019).

[29] X.-X. Hu, J.-Q. Wang, Y.-H. Yang, J. B. Surya, Y.-L. Zhang, X.-B. Xu, M. Li, C.-H. Dong, G.-C. Guo, H. X. Tang, and C.-L. Zou, All-optical thermal control for second-harmonic generation in an integrated microcavity, Opt. Express **28**, 11144 (2020).

[30] J.-Q. Wang, Y.-H. Yang, M. Li, X.-X. Hu, J. B. Surya, X.-B. Xu, C.-H. Dong, G.-C. Guo, H. X. Tang, and C.-L. Zou, Efficient Frequency Conversion in a Degenerate $\chi^{(2)}$ Microresonator, Phys. Rev. Lett. **126**, 133601 (2021).

[31] W. R. McGehee, W. Zhu, D. S. Barker, D. Westly, A. Yulaev, N. Klimov, A. Agrawal, S. Eckel, V. Aksyuk, and J. J. McClelland, Magneto-optical trapping using planar optics, New J. Phys. **23**, 013021 (2021).

[32] M. Kasevich and S. Chu, Atomic Interferometry Using Stimulated Raman Transitions, Phys. Rev. Lett. **67**, 181 (1991).

[33] A. Peters, K. Y. Chung, and S. Chu, Measurement of gravitational acceleration by dropping atoms, Nature **400**, 849 (1999).

[34] A. Peters, K. Y. Chung, and S. Chu, High-precision gravity measurements using atom interferometry, Metrologia **38**, 25 (2001).

[35] S.-K. Wang, Y. Zhao, W. Zhuang, T.-C. Li, S.-Q. Wu, J.-Y. Feng, and C.-J. Li, Shift evaluation of the atomic gravimeter NIM-AGRb-1 and its comparison with FG5X, Metrologia **55**, 360 (2018).

[36] L. Essen and J. V. L. Parry, An atomic standard of frequency and time interval: A casium resonator, Nature **176**, 280 (1955).

[37] B. de Beauvoir, F. Nez, L. Julien, B. Cagnac, F. Biraben, D. Touahri, L. Hilico, O. Acef, A. Clairon, and J. J. Zondy, Absolute Frequency Measurement of the $2S$-$8S/D$ Transitions in Hydrogen and Deuterium: New Determination of the Rydberg Constant, Phys. Rev. Lett. **78**, 440 (1997).

[38] P. Laurent, M. Abgrall, C. Jentsch, P. Lemonde, G. Santarelli, A. Clairon, I. Maksimovic, S. Bize, C. Salomon, D. Blonde, J. Vega, O. Grosjean, F. Picard, M. Saccoccio, M. Chaubet, N. Ladiette, L. Guillet, I. Zenone, C. Delaroche, and C. Sirmain, Design of the cold atom PHARAO space clock and initial test results, Appl. Phys. B **84**, 683 (2006).

[39] X. Liu, V. I. Yudin, A. V. Taichenachev, J. Kitching, and E. A. Donley, High contrast dark resonances in a cold-atom clock probed with counterpropagating circularly polarized beams, Appl. Phys. Lett. **111**, 224102 (2017).

[40] X. Liu, E. Ivanov, V. I. Yudin, J. Kitching, and E. A. Donley, Low-Drift Coherent Population Trapping Clock Based on Laser-Cooled Atoms and High-Coherence Excitation Fields, Phys. Rev. Appl. **8**, 054001 (2017).

[41] L.-M. Duan, M. D. Lukin, J. I. Cirac, and P. Zoller, Long-distance quantum communication with atomic ensembles and linear optics, Nature **414**, 413 (2001).

[42] D.-S. Ding, W. Zhang, Z.-Y. Zhou, S. Shi, G.-Y. Xiang, X.-S. Wang, Y.-K. Jiang, B.-S. Shi, and G.-C. Guo, Quantum Storage of Orbital Angular Momentum Entanglement in an Atomic Ensemble, Phys. Rev. Lett. **114**, 050502 (2015).

[43] Y. Wang, J. Li, S. Zhang, K. Su, Y. Zhou, K. Liao, S. Du, H. Yan, and S.-L. Zhu, Efficient quantum memory for single-photon polarization qubits, Nat. Photonics **13**, 346 (2019).

[44] R. Wen, C.-L. Zou, X. Zhu, P. Chen, Z. Y. Ou, J. F. Chen, and W. Zhang, Non-Hermitian Magnon-Photon Interference in an Atomic Ensemble, Phys. Rev. Lett. **122**, 253602 (2019).

[45] T. Bergeman, G. Erez, and H. J. Metcalf, Magnetostatic trapping fields for neutral atoms, Phys. Rev. A **35**, 1535 (1987).

[46] D. A. Steck, Rubidium 87 d line data, http://steck.us/alkalidata.

[47] E. Imhof, B. K. Stuhl, B. Kasch, B. Kroese, S. E. Olson, and M. B. Squires, Two-dimensional grating magneto-optical trap, Phys. Rev. A **96**, 033636 (2017).

[48] M. J. Snadden, J. M. McGuirk, P. Bouyer, K. G. Haritos, and M. A. Kasevich, Measurement of the Earth's Gravity Gradient with an Atom Interferometer-Based Gravity Gradiometer, Phys. Rev. Lett. **81**, 971 (1998).

[49] D. Savoie, M. Altorio, B. Fang, L. A. Sidorenkov, R. Geiger, and A. Landragin, Interleaved atom interferometry for high-sensitivity inertial measurements, Sci. Adv. **4**, eaau7948 (2018).

[50] A. Periwal, E. S. Cooper, P. Kunkel, J. F. Wienand, E. J. Davis, and M. Schleier-Smith, Programmable interactions and emergent geometry in an array of atom clouds, Nature **600**, 630 (2021).